S05

Proceedings of the 5th International Conference on Inverse Problems in Engineering: Theory and Practice, Cambridge, UK, 11-15th July 2005

A NEW IMPLEMENTATION OF THE ELLIPTIC SYSTEMS METHOD IN TIME DEPENDENT DIFFUSION TOMOGRAPHY APPLIED TO BACK REFLECTED AND TRANSMITTED DATA

Y.T. SHIH[1] and T.R. LUCAS[2]
[1] *Department of Applied Mathematics, National Chung-Hsing University,* Taichung 402, Taiwan
e-mail: yshih@amath.nchu.edu.tw
[2] *Department of Mathematics, University of North Carolina, Charlotte,* NC 28223, USA
e-mail: trlucas@uncc.edu

Abstract - It is common in applied work in engineering such as the search for buried land mines, or in medical imaging for diagnosis of possible breast tumors, to have only limited boundary measurement data, back reflected in the first case or transmitted in the second. Here we formulate the problem as one of coefficient recovery from incomplete boundary data in inverse problems. We have completed a new implementation of the Elliptic Systems Method (ESM) in time dependent diffusion tomography. The basic formulation of the ESM involves solving a system of (typically 4) coupled 4th-order PDE's, with the time variable integrated out using Legendre polynomials. Here, unlike the previous implementation that creates a larger (typically of size 8) mixed system of 2nd-order problems with quadratic elements over triangles, we use C^1 Bogner-Fox-Schmit bi-cubic elements over rectangles, with a new treatment of boundary conditions in the common case of incomplete boundary data. This new method is 4th-order accurate for sufficiently smooth functions. The new BC approach allows the use of homogeneous natural boundary conditions on parts of the boundary where no measured data is available. This combined effort is being reported elsewhere, but without extensive comparisons of difficult applications against the literature. Here we will focus on three previously published examples using back reflected or transmitted data with one or two inclusions. The new implementation in comparison gives markedly improved results for inclusion recovery, all of which are achieved without use of additional aids such as weight functions which have previously been thought to be essential. In addition the new implementation is shown to be surprisingly robust with respect to noise. We conclude with two examples illustrating the effect of increasing levels of noise.

1. INTRODUCTION

In this work we are using a diffusion PDE as an approximation for the more accurate transport PDE. The Elliptic Systems Methods (ESM) was originally introduced for the solution of inverse problems using time dependent data with just one source, but many detectors, in [11]. Many experiments, including the case of incomplete data collection, were reported in [12,13]. In this method the inverse problem is reduced to a system of overdetermined second-order boundary value problems (BVPs), with the time variable integrated out using Legendre polynomials. As one approach to resolve this over-determination, a fourth-order generalized biharmonic type equation was introduced to provide a well-posed problem. In [11-13] the 4th-order elliptic system was solved by using a mixed form of the FEM splitting the system into two adjoint system of 2nd-order PDEs which were then solved using quadratic elements over triangles. With the most standard number of such Legendre polynomials being four, this led to a coupled system of eight 2nd-order PDEs. It has been speculated that a more careful direct treatment of the solution of the *original* system of (usually four) biharmonic type PDEs, combined with other improvements and innovations, could potentially give significantly improved results.

In this paper we briefly describe such an implementation, and report on five numerical experiments. We use Bogner-Fox-Schmit bi-cubic elements over rectangles as our higher-order finite element to discretize the 4th elliptic system. In [13] it was found necessary to introduce a weighting function into the elliptic differential operator to successfully solve the incomplete data problems considered there. In this work, we simply directly solve the system, without use of any weighting function, a process that was found to be unsatisfactory in the implementation of [13]. We also introduce a new and more general approach to the BC's, along with a number of other innovations.

The focus point of interest in this paper, besides the details of the new implementation that will be developed primarily elsewhere, will be a detailed comparison of the results from [13] which explored the problem of coefficient recovery using limited data sets, primarily transmitted data alone or backscattered data alone. In addition, the new method has been found to be rather robust with respect to noise. Two

previously considered problems using just backscattered data will be considered at various noise levels up to 30% to see where and how they begin to fail. In one case there will be a single inclusion, and in the second rather more challenging case there will be two inclusions.

2. INVERSE PROBLEM AND ELLIPTIC SYSTEMS METHOD

Let $u(x,t)$ be the near infrared (NIR) light intensity. The PDE governing NIR light propagation in a turbid media is the transport parabolic equation. In [8] it was verified experimentally that the diffusion equation provides a very good description for NIR light intensity in biological tissues when the distance from the light source exceeds 7 times the transport mean free path. In this paper we will be using this diffusion approximation given as follows:

$$\begin{cases} u_t(x,t) &= \mathbf{div}(D(x)\nabla u(x,t)) - a(x)u(x,t), \quad x \in \mathbf{R}^2, t \in (0,T) \\ u(x,0) &= \delta(x-x_0), \end{cases} \tag{1}$$

where x_0 is the location of a single source, $D(x)$ is the diffusion coefficient and $a(x)$ is the absorption coefficient.

In practice NIR light propagates through a *bounded* domain Ω with heterogeneous material properties. We assume the boundary $\delta\Omega$ is piecewise smooth. It is common to approximate this model by applying Dirichlet BC's a certain distance out from the physical domain creating an extended problem over an artificial domain G past Ω [2]. We will assume for this paper that the diffusion D is constant, and that the absorption $a(x)$ is also constant except for certain inclusions in Ω located away from the boundary $\delta\Omega$. Thus let the absorption coefficient $a(x)$ be a smooth function that can be approximated by

$$a(x) = a_0 + h(x)$$

where a_0 is the background absorption coefficient for light transport through uniform media. The quantity $h(x)$ is a unknown perturbation of a_0 and estimating its locations and capacities (local integrals) will be our main focus. Now the problem for light propagating through this bounded domain during the time period $(0,T)$ may be re-described as:

$$\begin{cases} u_t(x,t) &= \mathbf{div}\left(D\nabla u(x,t)\right) - a(x)u(x,t) \quad x \in G, t \in (0,T), \\ u(x,0) &= \delta(x-x_0), \quad x \in G, x_0 \in G\backslash\Omega \\ u(x,t) &= 0, \quad x \in \partial G, t \in (0,T). \end{cases} \tag{2}$$

The above eqn.(2) will serve to model our *forward solver*. The inverse problem is to use time dependent data measured along part (incomplete data collection, which is the focus of this paper) or all of the boundary $\delta\Omega$ contained inside G as additional data to determine an approximation for the absorption perturbation $h(x)$. Towards this goal, Klibanov and Lucas [11-13] introduced the ESM to derive an iterative Newton-like method to recover $h(x)$ for a series of well posed boundary value problems involving a coupled system of elliptic PDE's. We briefly outline this method in the following.

First let us define the normalized function: $H(x,t) = u(x,t)/u_0(x,t) - 1$ for all $x \in \Omega$, $t \in (T_0, T_F)$. Next we let $u(x,t) = u_0(x,t)H(x,t) + u_0(x,t)$ and $a(x) = a_0 + h(x)$, and substitute these into (2), leading to [12]:

$$H_t(x,t) = \mathbf{div}(D\nabla H(x,t)) + 2D\frac{\nabla u_0(x,t)}{u_0(x,t)}\nabla H(x,t) - h(x) - h(x)H(x,t). \tag{3}$$

Let $p(x,t) = H_t(x,t)$ and differentiate eqn.(3) with respect to t. Hence

$$p_t(x,t) = \mathbf{div}(D\nabla p(x,t)) + 2D\frac{\partial}{\partial t}\left(\frac{\nabla u_0(x,t)}{u_0(x,t)}\nabla H(x,t)\right) - h(x)p(x,t), \tag{4}$$

thus eliminating the unknown perturbation $h(x)$, except for the last term, which could be dropped as a linearization, or used in an iterative Newton-like fashion as is done here. From values of $p(x,t)$, $H(x,t)$ can be easily recovered. From (3) the perturbation term $h(x)$ can be reconstructed by:

$$h(x) = \frac{1}{T_F - T_0}\int_{T_0}^{T_F}\left[\mathbf{div}(D\nabla H(x,t)) + 2D\frac{\nabla u_0}{u_0}\nabla H(x,t) - h(x)H(x,t) - H_t(x,t)\right]dt. \tag{5}$$

This iterative approach will be presented in more detail in Section 5.

The second step is to build a coupled system of elliptic PDE's to approximate eqn.(4) by use of a generalized Fourier series in t to numerically approximate $p(x,t)$. Let $\{l_k(t)\}_{k=1}^{\infty}$ be an orthonormal basis in $L^2(T_0,T_F)$ and $l_k(t)$'s functions constructed from the Legendre polynomials normalized over (T_0,T_F) to form this basis. Then for some positive integer $K>0$, $p(x,t)$ can be approximated well by the generalized Fourier series

$$p(x,t) \approx \sum_{i=1}^{K} l_i(t) q_i(x), \quad (x,t) \in \Omega \times (0,T), \tag{6}$$

where

$$q_i(x) = \int_{T_0}^{T_F} p(x,t) l_i(t) dt, \tag{7}$$

and we define $Q(x)$ as $[q_1(x), q_2(x), ..., q_K(x)]^T$.

Assume that the light intensity $u(x_i,t)$ can be measured with some detectors located at points x_i on the boundary of Ω during the time period $T_0 < t < T_F$. From this data the approximate light intensity, which we denote by $\psi(x,t)$, can be obtained along those parts of the boundary using interpolation, for example by cubic splines [4]. Then the boundary function $p(x,t)$ can be evaluated by:

$$p\mid_{\partial\Omega\times(T_0,T_F)} = \frac{\partial}{\partial t}\left(\frac{\psi}{u_0}\right) = \psi_1 \tag{8}$$

Next consider the boundary conditions for the function $Q(x)$. Let the vector $f(x) = [f_1(x), f_2(x), ..., f_K(x)]^T$ with $f_i(x)$ defined by

$$f_i(x) = \int_{T_0}^{T_F} \psi_1(x,t) l_i(t) dt \quad \text{for } i = 1,2,...,K \tag{9}$$

Following (4), (8) and (9), we obtain the following 2nd-order elliptic system:

$$\begin{cases} \boldsymbol{L}Q(x) &= 0, \quad x \in \Omega \\ Q\mid_{\partial\Omega} &= f(x) \\ \frac{\partial Q}{\partial n}\mid_{\partial\Omega} &= 0. \end{cases} \tag{10}$$

where $\boldsymbol{L}$ denotes a matrix operator with

$$\boldsymbol{L}Q(x) \equiv \mathbf{div}(D\nabla Q(x)) - \sum_{j=1}^{2} \boldsymbol{B}_j(x) \frac{\partial Q(x)}{\partial x_j} - (h(x)\boldsymbol{I} + \boldsymbol{C})Q(x), \tag{11}$$

and $\boldsymbol{I}$ being a $K \times K$ identity matrix. That $\frac{\partial Q}{\partial n}\mid_{\partial\Omega} \approx 0$ was argued in [12]. The $K \times K$ matrices $\boldsymbol{B}_1, \boldsymbol{B}_2$ and $\boldsymbol{C}$ depend on the ratio $\nabla u_0(x,t)/u_0(x,t)$, and for $1 \le k,s \le K$ they are given by

$$\begin{aligned} (\boldsymbol{B}_1, \boldsymbol{B}_2)_{k,s} &= -2D \int_{T_0}^{T_F} l_k(t) \frac{\partial}{\partial t}\left[\frac{\nabla u_0}{u_0} \int_0^t l_s(\tau)\, d\tau\right] dt \\ \boldsymbol{C}_{k,s} &= \int_{T_0}^{T_F} l_s'(t) l_k(t) dt. \end{aligned}$$

The system of eqns (10) is overdetermined since there are two boundary conditions rather than one. Various approaches can be used to take advantage of this to approximate $h(x)$. The approach taken by Klibanov and Lucas in the ESM [11-13] was to consider a 4th-order elliptic system by applying a formally adjoint operator to the PDE system, thus leading to a well-posed problem. Let $\boldsymbol{L}^*$ be the operator formally adjoint to $\boldsymbol{L}$ defined by

$$\boldsymbol{L}^* w(x) \equiv \mathbf{div}(D\nabla w(x)) + \sum_{j=1}^{2} \frac{\partial}{\partial x_j}\left(\boldsymbol{B}_j^T(x) w(x)\right) - (h(x)\boldsymbol{I} + \boldsymbol{C}^T) w(x).$$

Then we have the 4th-order system of coupled equations:

$$\left\{\begin{array}{lcl}(\boldsymbol{L}^*\boldsymbol{L})(Q(x)) &=& 0, \quad x\in\Omega\\ Q|_{\partial\Omega} &=& f(x)\\ \frac{\partial Q}{\partial n}|_{\partial\Omega} &=& 0\end{array}\right. \tag{12}$$

which is a well-posed problem having a unique solution. This system was solved in [11-13] by splitting it into a larger system of 2nd-order problems using C^0 elements over triangles.

3. A NEW IMPLEMENTATION OF THE ESM INCLUDING TREATMENT OF INCOMPLETE BC'S

In this section we develop the variational form for a high-order FEM to discretize the 4th-order coupled system of eqns (12) using C^1 elements over rectangles. In addition, we will consider the important practical case where boundary data for Q in (10) and (12) is only available on part of the boundary, a case we refer to as incomplete boundary data [13]. Let the boundary $\partial\Omega$ be divided into two regions (not necessarily connected): Γ_1, where measurements (data) are available, and Γ_2 where no measurements (data) are available, with $\partial\Omega = \Gamma_1 + \Gamma_2$. We will use essential BC's on Γ_1, fully using all available data, and zero natural BC's on Γ_2, which will be seen to be a reasonable choice. An alternative would be to assign zero values to the solution on Γ_2, as was done in [13], in the hope that the values on Γ_2 are sufficiently small due to their distance from the source that this would be a useful approximation in the absence of measured data values. In all cases we will assign $\frac{\partial Q}{\partial n}$ to be zero on all of the boundary $\partial\Omega$.

In the following variational formulation the test function v will be in the Sobolev space $H^2_{0,E}(\Omega)$ of functions whose partial derivatives up to the second-order are square integrable and satisfy the essential (E) BC's that $v|_{\Gamma_1} = 0$ and $\frac{\partial v}{\partial n}|_{\partial\Omega} = 0$. This corresponds to the assignment of known values to Q and $\frac{\partial Q}{\partial n}$, respectively. Let $w \equiv \boldsymbol{L}Q$ and introduce the notations $(w, v) = w^T v$ and $(n_1, n_2) = n$, the outward unit normal to $\partial\Omega$. Then

$$\begin{aligned}\int_\Omega (\boldsymbol{L}^* w, v)d\Omega &= \int_\Omega -D(\nabla w, \nabla v) - (w, \boldsymbol{B}_1 v_{x_1} + \boldsymbol{B}_2 v_{x_2}) - ((h\boldsymbol{I} + \boldsymbol{C}^T)w, v)d\Omega + \\ &\qquad \int_{\Gamma_2}\left(D\frac{\partial w}{\partial n} + (\boldsymbol{B}_1^T n_1 + \boldsymbol{B}_2^T n_2)w, v\right)dS \\ &= \int_\Omega (w, \mathbf{div}(D\nabla v) - \boldsymbol{B}_1 v_{x_1} - \boldsymbol{B}_2 v_{x_2} - (h\boldsymbol{I} + \boldsymbol{C})v)\, d\Omega + \\ &\qquad \int_{\Gamma_2}\left(D\frac{\partial w}{\partial n} + (\boldsymbol{B}_1^T n_1 + \boldsymbol{B}_2^T n_2)w, v\right)dS.\end{aligned}$$

Substituting $w = \boldsymbol{L}Q$ and recalling (11) we obtain

$$\int_\Omega (\boldsymbol{L}Q, \boldsymbol{L}v)d\Omega = 0 \quad \forall v \in H^2_{0,E}(\Omega) \tag{13}$$

$$Q|_{\Gamma_1} = f(x) \tag{14}$$

$$\frac{\partial Q}{\partial n}|_{\partial\Omega} = 0. \tag{15}$$

The natural BC that $D\frac{\partial(\boldsymbol{L}Q)}{\partial n} + (\mathbf{B}_1^T n_1 + \mathbf{B}_2^T n_2)\boldsymbol{L}Q$ equals zero follows as a consequence of the variational method using the space $H^2_{0,E}(\Omega)$, a result that seems very reasonable in light of (10).

Here we describe the FEM that will be applied to the above variational form of the system (12) as generalized above to the case of incomplete boundary data. There are several articles which discuss the solution of biharmonic problems by higher-order FEM's [1,5,6,7,9,10]. In this paper, we consider a C^1-finite element approximation for a system of 4th-order biharmonic like PDE's. Assume Ω is a rectangular domain which is partitioned into $m\times n$ smaller rectangular meshes Ω_i and $\Omega = \bigcup_{i=1}^{m\times n}\Omega_i$. Each rectangular mesh is affine equivalent to the reference domain $[0,1]\times[0,1]$ of $\overline{\Omega}_i$. Since the differential operator $\boldsymbol{L}$ is of fourth-order, we choose the Bogner-Fox-Schmit (BFS) rectangle [7], which is a finite element of class C^1, to obtain the discrete problem.

Let (ζ, η) be a generic element of $\overline{\Omega}$. Denote the approximate solution Q^h by $[q_1^h, q_2^h, ..., q_K^h]^T$ for some positive K in the Legendre approximation of $p(x,t)$. The 16 degrees of freedom characterizing this element are Q^h's values as well as $\frac{\partial Q^h}{\partial x_1}$, $\frac{\partial Q^h}{\partial x_2}$, $\frac{\partial^2 Q^h}{\partial x_1 \partial x_2}$ at each vertex of $\overline{\Omega}$. For the 2-D reference mesh, the

shape functions are defined by a combination of the above shape functions. Thus integration on each mesh can be transformed into the reference mesh which is easily evaluated on $\overline{\Omega}$ as

$$\int_{\Omega_i} (\boldsymbol{L}Q^h(x,y), Lv(x,y))dxdy = \int_0^1 \int_0^1 (\boldsymbol{L}Q^h(\zeta,\eta), \boldsymbol{L}v(\zeta,\eta))|\boldsymbol{J}|d\zeta d\eta, \text{ where } |\boldsymbol{J}| \text{ is a Jacobian.} \quad (16)$$

We use the 4×4 Gaussian quadrature rule to evaluate the above integration. Assume $[z_1^j, z_2^j, z_3^j, z_4^j]$ represent the unknowns at node j represented $Q^h, Q^h_{x_1}, Q^h_{x_2}, Q^h_{x_1,x_2}$. Because Q^h can be approximated by the equation

$$Q^h(\zeta,\eta) = \sum_{1 \le i,j \le 4} N_i^j z_i^j \quad (17)$$

each computational grid has 16 degrees of freedom and this leads to a system of 16×16 coupled equations when evaluating eqn.(16).

Furthermore, this finite element space can achieve up to 4th-order accuracy. Because of this high accuracy in the solution, we will be able to prolong the recovered perturbation h from coarser grids into finer grids, saving considerable computing time. This will be discussed in the next section.

4. PROLONGATION

For minimizing computing time, after computing the Q^h's using eqn.(12) on a coarse mesh we increase the resolution of the reconstructed image through the eqn.(5) by using a prolongation method. This achieves a higher quality recovery of $h(x)$. The solution Q^h derived by the Bogner-Fox-Schmit scheme belongs to C^1, so it's natural to obtain the exact values of $Q^h, Q^h_{x_1}, Q^h_{x_2}, Q^h_{x_1,x_2}$ inside a finer grid using exact values of the trial functions on the reference mesh. This leads us to implement a prolongation for finer meshes using (17). This also makes it easy to evaluate interior values for a more accurate $h(x)$ recovery. We use bicubic spline interpolation to approximate the values of $h(x)$ using the refined mesh points.

5. IMAGE RECONSTRUCTION ALGORITHM

The coupled system (12) is nonlinear since the solution Q depends on an unknown $h(x)$ term. Here we consider a Newton-like algorithm to solve the above system of equations. Our image reconstruction algorithm can be described as follows:

1. Construct the BC $f(x)$ by interpolating the data readings from the detectors.
2. Let the initial perturbation term be $h^{(0)}(x) = 0$, using given values of T_0, T_F.
3. For $n = 1, 2, 3, ...$
   (a) Denote $\boldsymbol{L}^{(n)}Q(x) \equiv \mathbf{div}(D\nabla Q(x)) - \sum_{j=1}^2 \boldsymbol{B}_j(x)\frac{\partial Q(x)}{\partial x_j} - \left[h^{(n-1)}(x)\boldsymbol{I} + \boldsymbol{C}\right] Q(x)$.
   (b) Discretize the corresponding variational problem (13)-(15) using finite elements over Boger-Fox-Schmit rectangles [7].
   (c) Solve the resulting linear system by Cholesky factorization.
   (d) Evaluate $H^{(n)}(x,t) = \sum_{k=1}^K \int_0^t l_k(\tau)d\tau Q_k^{(n)}(z(x))$.
   (e) Reconstruct the image using
   $h^{(n)}(x) = \frac{1}{T_F - T_0}\int_{T_0}^{T_F} [\mathbf{div}(D\nabla H^{(n)}(x,t)) + 2D\frac{\nabla u_0}{u_0}\nabla H^{(n)}(x,t) - h^{(n-1)}(x)H^{(n)}(x,t) - H_t^{(n)}(x,t)]dt$.

6. NUMERICAL SIMULATION

In this section we compare with the numerical experiments of [13]. In all cases the computational region for the forward solver will be G=$[-105, 105] \times [-40, 40]$ with units in mm, assuming an envelope of size 5 mm. The inverse solver will be applied to the region Ω=$[-100, 100] \times [-35, 35]$. The source will be located at $(40, 35)$, on the upper right side. We add 1% multiplicative Gaussian noise to the detector readings, meaning we use a distribution with mean zero and standard deviation $\sigma = 0.005$. The homogeneous background values for the mean free path of scattering and absorption are l_t=1.0 mm and $l_a = 250$ mm, which are equivalent to diffusion and absorption coefficients of $D = 0.075$ mm^2/ps, and $a = 0.0009$ ps^{-1}. Here we use a computation mesh of 65×33 with a prolongation to 256×256. We will use in all cases the values $T_0 = 3000$ ps and $T_F = 9000$ ps.

We placed 41 uniformly distributed detectors on both horizontal sides of the rectangle Ω, and used *selected* readings from these varying with the simulation. In each numerical experiment the detectors where data is used are both identified by intervals and also marked by small black dots in the corresponding figure. The (fixed) source position is marked with a large star. Cubic spline interpolation was used to recover values in between detector locations. Outside these intervals, natural BC's were used as described in Section 3.

We selected cylindrical inclusion(s) with a radius of 3 mm. These are marked as a black ring inside all figures to represent the correct position of the target inclusion. For a measurement of accuracy, we denote *Dev* be the distance between the location of the maximum recovered value of the inclusion and the actual inclusion center.

For Numerical Experiments 1 - 3, we have simulated a single inclusion of radius 3 mm with $h(x) = 0.0045$, and constant scattering coefficient. The data was collected either on the top (back reflected information) or on the bottom (transmitted) side. We also consider the case of two inclusions using back reflected data. The stopping criterion for the Newton-like iteration is a change of no more than 2% in the relative error over the reportage region from one iteration to the next.

In Numerical Experiments 4 - 5, we are challenging the robustness of our code by increasing the noise levels from 5% to 30% observing how and when the method fails. As the noise level is increased, the approximation of $p(x,t)$ will cause some difficulties for the convergence of the Newton-like algorithm. Here we add one more criterion for stopping: stop if there is an increase in the relative error after iteration number 6.

Numerical Experiment 1: Transmitted data. In the first test we chose an interval of $(-85, 20)$ on the bottom side. The simulated inclusion was located at $(-10, -10)$. Figure 1 shows the reconstructed image with reported center $(-12.5, -10.9)$ with *Dev*= 2.66 mm while in [13] it was reported at $(-12.5, -13.1)$, with *Dev*= 3.98 mm. In [13] it was necessary to use a weight function applied in the region $[-65, 27] \times [-25, 30]$ to control the reconstructed image. We have a similar image quality to that of [13], but with a superior center. In [13] if no weight function had been used the image was reported to be unsatisfactory, with a center of $(-12.5, -17.5)$, *Dev*= 7.91 mm.

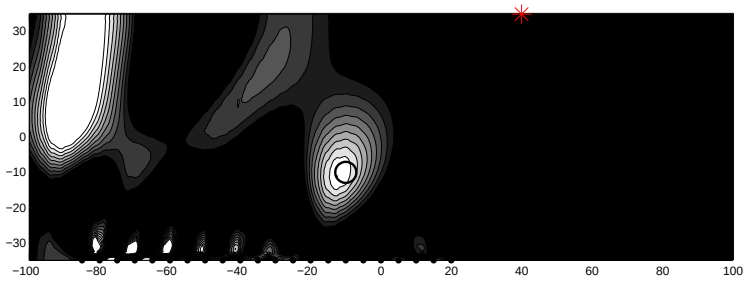

Figure 1: Recovered Inclusion and detector positions for Test 1: 1% Gaussian noise using transmitted detectors. The center of the image is reported at $(-12.5, -10.9)$ improving on $(-12.5, -13.1)$.

Numerical Experiment 2: Back reflected data. In the second test we used back reflected data on the interval $(-85, 20)$ on the top side. The inclusion has the same geometry as in Numerical Experiment 1, but the center location has been moved upward to $(-10, 10)$. Figure 2*a* shows the reconstructed image with reported center $(-13.3, 10.7)$, *Dev*= 3.40 mm. In this case we have much better results in image quality. In [13] the center was reported at $(-12.5, 13.1)$, *Dev*= 3.98 mm by using a weight function.

Numerical Experiment 3: Two inclusions using back reflected data. Here we added a second inclusion at the location $(-50, 10)$ again with a radius of 3 mm and the same value as before. The detectors are the same back reflected ones as before. Figure 2*b* shows the reconstructed image with reported center $(-50.8, 6.3), (-13.3, 10.7)$, *Dev*= 3.79, 3.37, respectively. In [13], using the weight function the centers were reported at $(-56.2, 10.9), (-12.5, 13.1)$, with the considerably larger values of *Dev*= 6.26, 3.98, respectively. Without the weight function in [13], the results were reported as $(-54.7, 22.4), (-3.1, 3.3)$ with *Dev*= 13.3, 9.6.

Numerical Experiment 4: Back reflected data at various levels of noise with a single inclusion. Here we use the same conditions as in Numerical Experiment 2, but tested various Gaussian noise levels: 5%, 10%, 15%, 20%, 25%, 30%. All reconstructed images are shown in Figure 3. For purposes of convenience and reportage, a visually identified region of $(-12, 12) \times (-25, 5)$ is used for the application of watching region. Inside this region there is reportage on 5 expressions: X_0, Y_0, *Max*, *Dev* and *Cap*, where (X_0, Y_0) gives the location of the maximum recovered value of the inclusion. There is an increasing realization [13] that while it is difficult to recover the correct geometry and magnitude of the inclusion separately, the recovery of the capacity, defined as the product of the volume and the absorption perturbation, is more achievable. This recovery is reported as *Cap* in Table 1. The correct *Cap* value is 0.127 for all experiments. As our recovery results vary in space, our calculations are evaluated by numerical integration. From an inspection of Figure 3, it appears that in this example the method deteriorates gradually with increasing noise, becoming progressively less satisfactory as noise increases from 10%.

Noise	*Max*	(X_0, Y_0)	*Dev*	*Cap*
1%	0.291E-3	(-13.3,10.7)	3.40	0.098
5%	0.322E-3	(-13.3,10.9)	3.42	0.099
10%	0.385E-3	(-13.3,10.6)	3.35	0.112
15%	0.440E-3	(-13.3,10.7)	3.40	0.137
20%	0.511E-3	(-13.3, 8.5)	3.62	0.154
25%	0.540E-3	(-13.3, 8.5)	3.62	0.164
30%	0.624E-3	(-15.6,-4.9)	15.81	0.178

Table 1: Performance measurements for various noise levels using back reflected detectors. The correct *Cap* value was 0.127, with center of $(-10, 10)$.

Numerical Experiment 5: Back reflected data at various levels of noise with 2 inclusions. Here we use exactly the same conditions as in Numerical Experiment 3, but increase the noise level up to 20%. The results are shown in Table 2 and Figure 4. Our recovery fails for the left inclusion when the noise level is somewhere between 5% and 10%.

	incl. (-10,10), Cap=0.127				incl. (-50,10), Cap=0.127			
Noise	*Max*	(X_0, Y_0)	*Dev*	*Cap*	*Max*	(X_0, Y_0)	*Dev*	*Cap*
1%	0.29E-3	(-13.3,10.7)	3.37	0.101	0.37E-3	(-50.8, 6.3)	3.79	0.128
5%	0.33E-3	(-13.3,10.7)	3.37	0.103	0.31E-3	(-47.7, 8.5)	2.75	0.105
10%	0.39E-3	(-13.3,10.7)	3.37	0.122	0.31E-3	(-44.5,10.7)	5.54	0.085
15%	0.46E-3	(-13.3,10.4)	3.32	0.136	0.40E-3	(-61.7,18.6)	14.5	0.075
20%	0.52E-3	(-13.3, 8.5)	3.62	0.157	0.53E-3	(-61.7,18.3)	14.3	0.077

Table 2: Performance measurements for 2 inclusions under various noise levels using back reflected detectors.

7. CONCLUSIONS

A new implementation of the ESM is presented using C^1-finite elements over Boger-Fox-Schmit rectangles. In addition, a novel treatment of incomplete boundary data is developed and applied. Comparisons with previously published results using incomplete boundary data, both of transmitted and back reflected type, are made. The implementation is shown to markedly improve the quality of the results in two important ways: more accurate centers and no need to use a weighting function. In the previous work, the results with the base method, without use of a weighting function, were unacceptable. In addition, the method is shown to accept remarkably high levels of noise. It is our opinion that the markedly improved quality is due to a combination of improved approaches in the new implementation, including use of: a

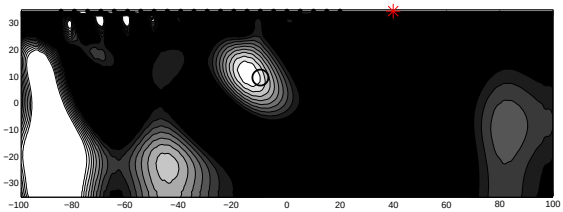

(a) Numerical Experiment 2: One Inclusion, back reflected.

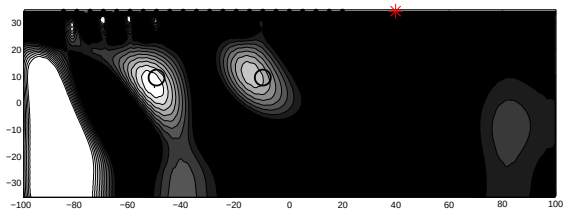

(b) Numerical Experiment 3: Two Inclusions, back reflected.

Figure 2: Recovered Inclusion(s) for Numerical Experiments 2 and 3 using 1% Gaussian noise. The positions of the back reflected detectors and the source are also shown.

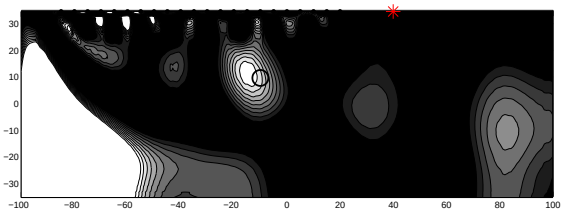

(a) 5% noise

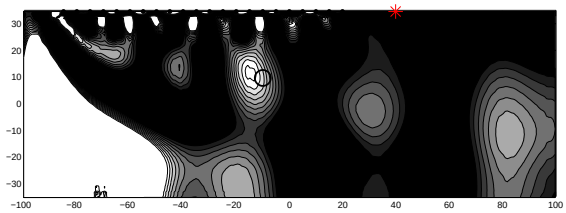

(b) 10% noise

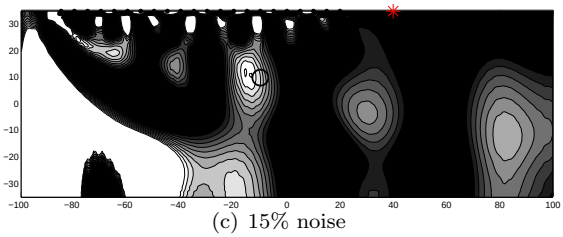

(c) 15% noise

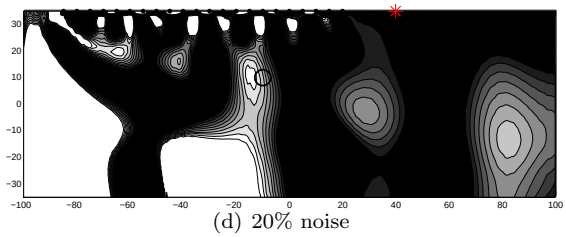

(d) 20% noise

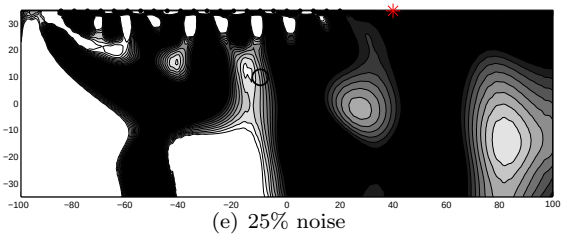

(e) 25% noise

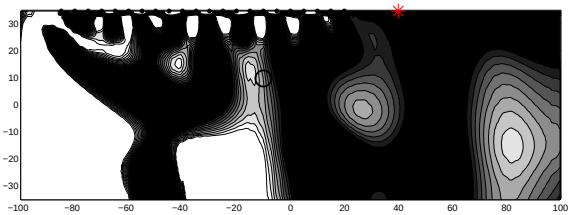

(f) 30% noise

Figure 3: One recovered inclusion and detector position for Numerical Experiment 4: Gaussian noise of 5%, 10%, 15%, 20%, 25%, 30% using back reflected detectors.

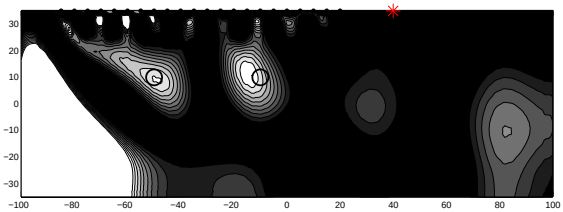

(a) 5% noise

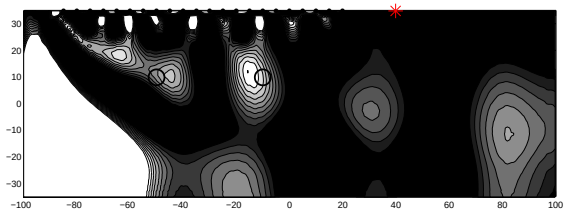

(b) 10% noise

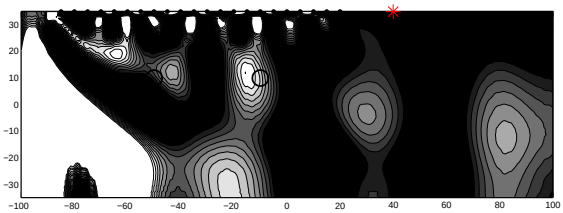

(c) 15% noise

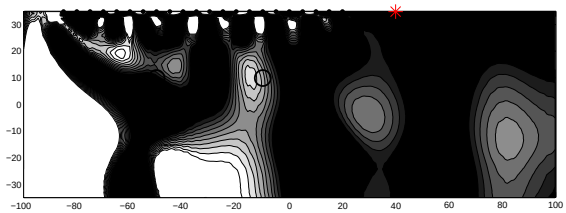

(d) 20% noise

Figure 4: Two recovered inclusions and detector positions for Numerical Experiment 5: Gaussian noise of 5%, 10%, 15%, 20% using back reflected detectors.

more sophisticated fourth-order FEM method, a more general treatment of the boundary conditions, and a variety of other additional factors.

Acknowledgement

The National Science Council of Taiwan Government is acknowledged for its support in part by grant NSC 93-2115-M-005-008.

REFERENCES

1. I. Altas, J. Dym, M. Gupta and R. Manohar, Multigrid solution of automatically generated high order discretizations for the biharmonic equation. *SIAM J. Sci. Comput.* (1998) **19**, 1575-1585.

2. S. Arridge, Optical tomography in medical imaging, Topical review. *Inverse Problems* (1999) **15**, R41-R93.

3. G. Bal, Optical tomography for small volume absorbing inclusions. *Inverse Problems* (2003) **19**, 371-386.

4. C. de Boor, *A Practical Guide to Splines,* Springer-Verlag, New York, 1978.

5. A. Brandt and J. Dym, Effective boundary treatment for the biharmonic Dirichlet problem, *Proc. Seventh Copper Mountain Conference on Multigrid Methods*, (eds. N.D. Melson, T.A. Manteuffel, S.F. McCormick and C.G. Douglas), NASA Conference Publication,1996, **CP 3339**, pp.97-107.

6. J. Bramble and X. Zhang, Multigrid methods for the biharmonic problem discretized by conforming $\mathcal{C}^1$ finite element on nonnested meshes. *Numer. Funct. Anal. and Optimiz* (1995) **1**, 835-846.

7. P.G. Ciarlet, *The Finite Element Method for Elliptic Problems*, Studies in Mathematics and its Applications, **4**, North-Holland, 1978.

8. B. B. Das, F. Liu and R. R. Alfano, Time-resolved fluorescence and photon migration studies in biomedical and model radom media. *Rep. Prog. Phys.* (1997) **60**, 227-292.

9. M.A. Diaz and I. Herrera, Indirect method of collocation for the biharmonic equation, *Fourteenth International Conference on Domain Decomposition Methods*, (eds. I. Herrera, D. E. Keyes, O. B. Widlund and R. Yates), Cocoyoc, Mexico, 2003, pp.249-256.

10. L.M. Fernandes, I.N. Figueiredo and J.J. Judice, On the solution of a finite element approximation of a linear obstacle plate problem. *Int. J. Appl. Math. Comput. Sci.* (2002) **12**(1), 27-40.

11. M.V. Klibanov, T.R. Lucas and R. M. Frank, A fast and accurate imaging algorithm in optical/diffusion tomography. *Inverse Problems* (1997) **13**, 1341-1361.

12. M.V. Klibanov and T.R. Lucas, Numerical solution of a parabolic inverse problem in optical tomography using experimental data. *SIAM J. Appl. Math.* (1999) **59**, 1763-1789.

13. M.V. Klibanov and T.R. Lucas, Elliptic systems method in diffusion tomography using back-reflected data. *Inverse Problems* (2000) **16**, 199-221.

14. X.D. Li, M.A. O'Leary, D.A. Boas, B. Chance and A.G.Yodh, Fluorescent diffuse photon density waves in homogeneous and heterogeneous turbid media: analytic solutions and applications. *Appl. Optics* (1996) **35**, 3746-3758.